Heterodimers: Plasmonic Properties of Mismatched Nanoparticle Pairs

Lisa V. Brown,[†,∥] Heidar Sobhani,[‡,∥] J. Britt Lassiter,[§,∥] Peter Nordlander,[‡,§,∥,*] and Naomi J. Halas[†,‡,§,∥,*]

[†]Department of Chemistry, [‡]Department of Electrical and Computer Engineering, [§]Department of Physics and Astronomy, and [∥]Laboratory for Nanophotonics, Rice University, Houston, Texas 77005

ARTICLE

ABSTRACT Heterodimers—two closely adjacent metallic nanoparticles differing in size or shape—exemplify a simple nanoscale geometry that gives rise to a remarkably rich set of properties. These include Fano resonances, avoided crossing behavior, and a surprising dependence of the scattering spectrum on the direction of excitation, known as the "optical nanodiode" effect. In a series of studies, we experimentally probe and theoretically analyze these properties in heterodimer nanostructures, where nanoparticle size and plasmon resonance frequency are varied systematically. Polarization-dependent dark-field microspectroscopy on individual heterodimer structures fabricated using a novel electromigration assembly method allows us to examine these properties in detail. These studies expand our understanding of the range of physical effects that can be observed in adjacent metallic nanoparticle pairs.

KEYWORDS: dimer · Fano resonance · diode effect · plasmon hybridization · electrostatic self-assembly

The electron oscillations in metal nanoparticles, known as surface plasmons, dominate the optical response of individual nanoparticles. When two metal nanoparticles are placed in close proximity to each other, the properties of their surface plasmons are dramatically modified.[1−5] This configuration of nanoparticles is known as a "dimer" since the surface plasmons of the individual nanoparticles mix and hybridize in direct analogy with the molecular orbital theoretical description of the quantum states of diatomic molecules.[6] Also in analogy with diatomic molecules, nanoparticle pairs can be formed[7] from nanoparticles with indistinguishably identical properties—homodimers—or pairs of metallic nanoparticles with differing properties—heterodimers. The homodimer has been studied extensively.[2,3,6,8−20] In this structure, the plasmon coupling increases with decreased interparticle spacing, resulting in red-shifted energies of the hybridized modes[6,13,17] until the quantum regime is obtained, where electron tunneling between the adjacent nanoparticles alters the classical response.[21,22] This structure is of extreme interest for surface-enhanced Raman spectroscopy applications due to the high-intensity "hot spot" formed in the junction between nanoparticles when light polarized along the interparticle axis excites the dimer plasmon.[23−31]

In contrast, the plasmonic heterodimer is not nearly as well-studied or understood. We can anticipate that this structure would give rise to new physical effects not seen in matched nanoparticle pairs. While plasmonic nanostructures can support both bright and dark modes,[32] symmetry-breaking relaxes selection rules and enhances coupling between all of the plasmon modes of a nanostructure.[33,34] In the case of two adjacent, mismatched nanoparticles, this allows modes with different characteristics, such as angular momentum or line shape, to interact strongly with each other. These interactions can be a strong function of interparticle distance, resulting in energy shifts and avoided crossings of the plasmon modes as the constituent nanoparticles coalesce into the dimer structure. Interactions between broad and narrow resonant modes can occur, resulting in a Fano resonance with its characteristically asymmetric line shape. While first observed in atomic systems, Fano resonances have recently become evident in a wide range of optical media, including excitonic systems, metamaterials, and plasmonic structures.[35−41] Fano resonances in plasmonic media are of particular interest because they are extraordinarily sensitive to their local dielectric environment. This sensitivity may be exploitable in the development of ultrasensitive chemical or

*Address correspondence to nordland@rice.edu, halas@rice.edu.

Received for review November 30, 2009 and accepted January 14, 2010.

Published online January 21, 2010.
10.1021/nn9017312

biological nanosensors that show large optical effects in response to individual molecular binding events. The low scattering intensities associated with Fano resonances make these modes of interest also in plasmonic waveguide applications. Another property specific to heterodimers is the "optical nanodiode" effect.[42] For two different, closely adjacent nanoparticles excited with optical polarization transverse to the interparticle axis, the optical response of the nanoparticle pair may differ depending upon the direction of incident light. This effect results from the asymmetric excitation of the pair of nanoparticles in series, where the incident field exciting the second nanoparticle arises both from far-field incident light and from the near-field response of the first nanoparticle. The asymmetry, which is a characteristic feature of heterodimers, may enable the design of nanoscale photonic diodes in nanophotonic circuits.

Size and shape variations of nanoparticles or nanostructures that occur naturally within typical fabrication methods provide sufficient structural variation to result in frequent occurrences of mismatched nanoparticle or nanostructure pairs. The assembly of heterogeneous pairs of plasmonic nanoparticles with detuned resonant properties offers a practical and systematic method to explore this regime in experimentally realizable nanostructures. In this article, we describe a series of studies of the optical properties of individual plasmonic heterodimers. Two types of heterodimer structures were studied: (1) dimers consisting of two solid Au nanoparticles, where the relative nanoparticle size was varied, and (2) dimers consisting of one solid Au nanoparticle in close proximity to a silica−Au nanoshell, where the solid Au nanoparticle size was varied. The heterodimers were assembled using an electromigration method developed for this purpose, which results in the coalescence of isolated, individual nanoparticle pairs on a dielectric substrate. The heterodimers were studied using polarization-dependent dark-field microspectroscopy, correlated with scanning electron microscopy images of each dimer. This combination of physical measurements allows us to study, in a systematic manner, how heterodimer properties such as Fano resonances and the optical nanodiode effect depend on the geometric properties of the heterodimer and its constituent nanoparticles.

RESULTS AND DISCUSSION

Heterodimer Fabrication and Assembly. The dimers fabricated and utilized in this study consisted of solid Au spherical nanoparticles (NPs) and Au nanoshells (NSs).[43,44] NPs with radii of 25, 50, and 75 nm were purchased from Ted Pella, Inc. To remove excess surfactant molecules, the colloidal suspensions were centrifuged and resuspended in deionized water. Silica nanoparticles with radii of 60 nm (Precision Colloid, 50 wt %) were used as cores for NSs, which were fabricated by a previously reported method where CO was used as the reducing agent for chemical deposition of the metallic shell.[45,46] The NSs were then rinsed by centrifugation and resuspended in deionized water.

The dimer synthesis and sample preparation are illustrated schematically in Figure 1. Combinations of NP and NS suspensions, which ultimately determined the composition of the heterodimers, were mixed in 1:1 volumetric ratios. Each mixture was deposited onto a glass coverslip functionalized with 3-aminopropyltriethoxysilane (APTES). After deposition, the substrate-bound nanoparticles still remained predominantly discrete, due to the electrostatic repulsion of their charged surfaces. The nanoparticles were then functionalized with 11-mercaptoundecanol (MUOH), which partially neutralized their surface charge. Following MUOH functionalization, the nanoparticles coalesced on the substrate. After 8−24 h, the nanoparticles had migrated along the substrate, having formed dimers and other small aggregates; however, their distribution on the substrate was too dense for dark-field microspectroscopy on individual aggregate structures. Therefore, all particles were removed from the substrate by sonication in deionized water, which resulted in a very stable suspension of dimers and other aggregates. The particles were redeposited onto a glass coverslip that was functionalized with poly(4-vinyl pyridine) (PVP) and patterned with alignment markings. These markings allowed us to determine the exact location and orientation of individual dimers by using environmental scanning electron microscopy (ESEM, FEI Quanta 400). Further details of the dimer synthesis procedure are provided in the Supporting Information (Figures S1 and S2).

High-resolution ESEM images of the specific dimers studied are shown in Figure 2. These consist of three NP−NP heterodimers (Figure 2A−C) and three NP−NS heterodimers (Figure 2D−F). In both sequences, the size of a Au nanosphere (nanoparticle 1) is varied, while the size of the adjacent nanoparticle (nanoparticle 2) is essentially held constant. In sequence A−C, nanoparticle 2 is a solid nanosphere; in sequence D−F, nanoparticle 2 is a silica−Au nanoshell. Although dimer C is technically a homodimer, we will refer to these nanostructures collectively as heterodimers A−F in the subsequent discussion of their properties.

Spectroscopic analysis of each dimer was performed using an inverted dark-field microscope equipped with a polarizing filter and a spectrometer.[13] The incident beam consisted of s-polarized white light from a halogen lamp, and the angle of polarization parallel to the plane of the sample was adjusted by rotating the sample stage. Scattering spectra were obtained with light polarized parallel and perpendicular to the dimer axis. For each polarization angle, two measurements were obtained, with the k-vector of the incident light oriented in opposite directions, resulting in a total of four polarized scattering spectra for each dimer.

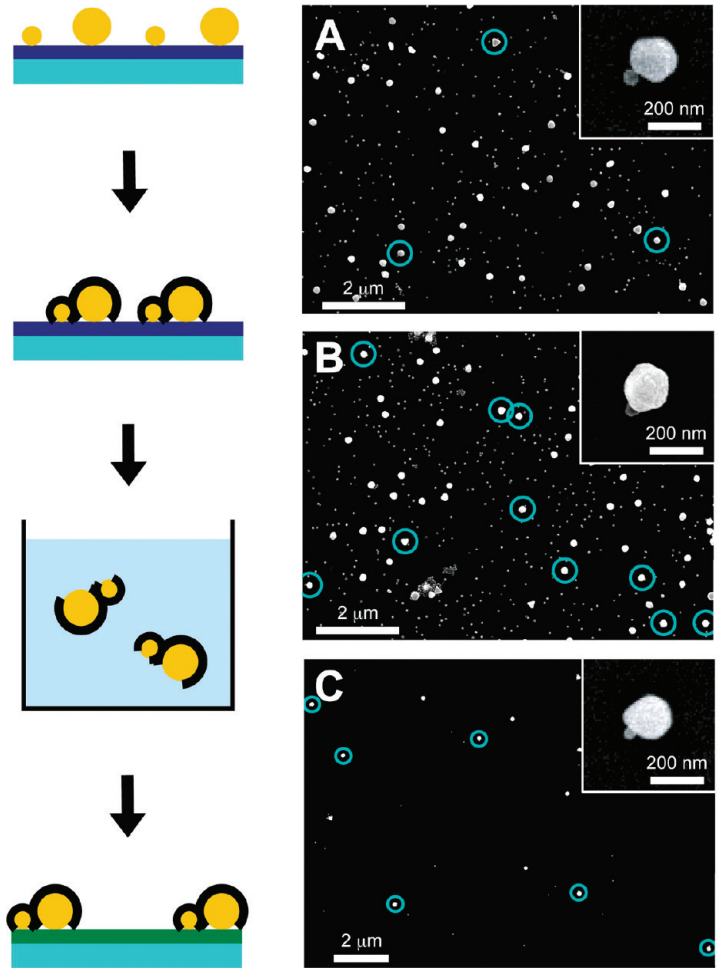

Figure 1. Schematic diagram of heterodimer synthesis. A 1:1 mixture of NPs and/or NSs is deposited onto a glass coverslip functionalized with APTES (dark blue). The nanoparticles are functionalized with MUOH (black) and then released into water *via* sonication. They are redeposited onto a glass coverslip functionalized with PVP (green). SEM images of (A) nanoparticle deposition onto APTES, (B) MUOH functionalization, and (C) dimer deposition onto PVP.

Electromagnetic Simulations. Scattering spectra of the heterodimers studied experimentally were calculated using the finite difference time domain (FDTD) method. In each simulation, the nanoparticles in each dimer were surrounded by a 2 nm dielectric layer with $\varepsilon = 2.25$, corresponding to the MUOH layer adhering to each structure. To achieve the closest possible agreement between our simulations and the experimentally obtained spectra, a realistic dielectric function for Au was used (JC).[47] The heterodimers were simulated on a dielectric substrate[48] with $\varepsilon = 2.25$, with the dimer axis parallel to the dielectric surface.

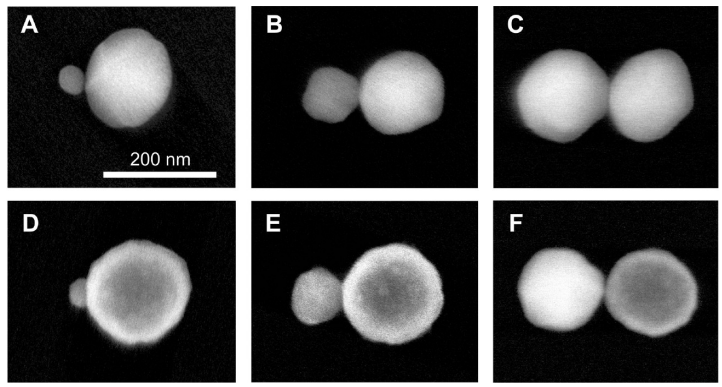

Figure 2. ESEM images of six individual dimers to be discussed in this paper. Dimers are on PVP-functionalized glass. Nanoparticles (NPs) are identified by facets and uniform contrast. Nanoshells (NSs) are identified by non-uniform contrast due to the thin Au shell. (A−C) NP−NP heterodimers; (D−F) NP−NS heterodimers. See Table 1 for specific dimensions of the nanoparticles used in FDTD simulations.

TABLE 1. Dimensions of Heterodimers in FDTD Simulations

dimer	nanoparticle 1	nanoparticle 1 radius (nm)	nanoparticle 2	nanoparticle 2 inner radius (nm)	nanoparticle 2 outer radius (nm)	gap size (nm)
A	NP	24	NP		76, 90[a]	2
B	NP	50	NP		76	4
C	NP	76	NP		76	2
D	NP	24	NS	66	84	2
E	NP	50	NS	66	84	4
F	NP	76	NS	66	84	2

[a]Minor and major axes, respectively.

All nanoparticles were assumed to be spheres, except nanoparticle 2 in heterodimer A, which was modeled as a prolate spheroid, in agreement with the ESEM image of this structure (Figure 2A). This adjustment was necessary because the scattering spectrum of a prolate particle is broader and more red-shifted than that of a spherical particle when the incident light is polarized parallel to the major axis (Supporting Information Figure S3).

The interparticle gap of each heterodimer was determined by the geometry resulting in the best agreement between the experimentally obtained and calculated dimer spectra. As the size of the gap decreases, the scattering spectrum red shifts when the incident light is polarized parallel to the dimer axis.[6,19] With extremely small gaps and touching particles, many plasmon modes can be identified.[19] In this study, touching particles can be excluded because each particle is coated with a layer of MUOH molecules, and the experimental spectra agree with simulations in which the interparticle gap is 2−4 nm (Figure S3). The specific dimensions of the heterodimers used in our simulations are listed in Table 1.

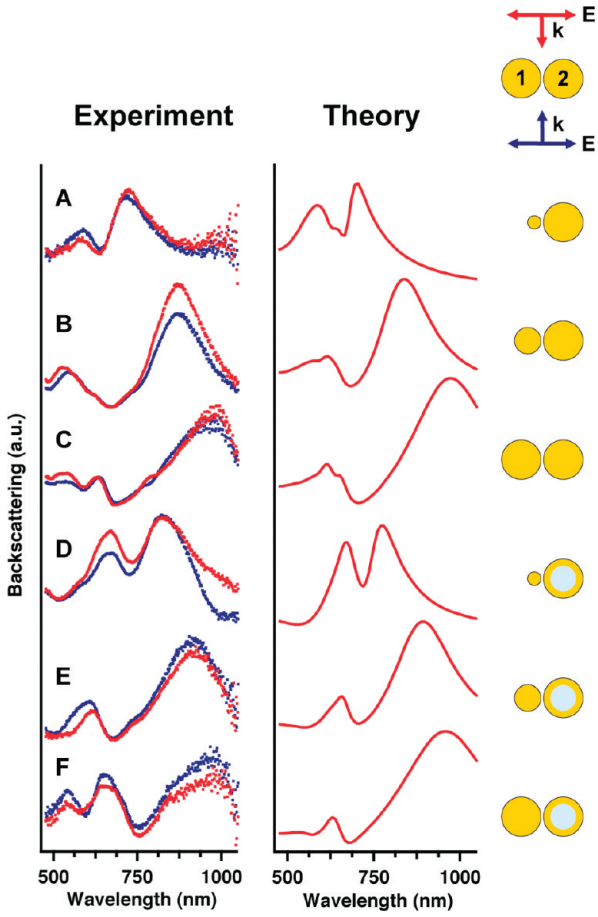

Figure 3. Experimental and theoretical scattering spectra for heterodimers A−F with longitudinally polarized incident light. Because the spectra for opposing k-vectors are identical due to symmetry, theoretical spectra include only one direction of propagation. Dimensions for each dimer simulation are given in Table 1.

To simulate the optical excitation and collection geometries in our experiments, the incident light in our simulations was s-polarized with the k-vector parallel to the substrate, where the incident polarization angle was adjusted slightly to achieve optimal agreement between experimental and theoretical spectra. Scattered light from the simulations was collected in a 64° angular cone above the nanostructure, corresponding to the collection angle defined by the dark-field objective used in the experiments (NA = 0.9).

Longitudinal Excitation of Heterodimers. When the incident beam is polarized parallel to the dimer axis, the plasmon modes of the constituent nanoparticles hybridize, forming bonding and antibonding[49] heterodimer plasmon modes. The experimental and theoretical scattering spectra for heterodimers A−F for excitation along the interparticle axis are shown in Figure 3. The spectra are displayed sequentially for direct comparison between the coupling of the smaller, size-dependent Au nanosphere (nanoparticle 1) to the adjacent Au nanosphere (A−C) or Au nanoshell (D−F) (nanoparticle 2).

It is immediately apparent upon comparison of these spectra that the plasmonic properties of a solid nanosphere coupled to either a second nanosphere (A−C) or to a nanoshell (D−F) are remarkably similar. This striking resemblance indicates that the plasmon modes of nanoparticle 1 couple primarily with the plasmon modes associated with the outer surface of nanoparticle 2. In each spectrum, two main features can be identified: a large, broad peak between 800 and 1000 nm in wavelength and a smaller peak appearing at a wavelength of nominally 600 nm. As the size of nanoparticle 1 is increased, the larger peak broadens and red shifts, while the smaller peak essentially retains its spec-

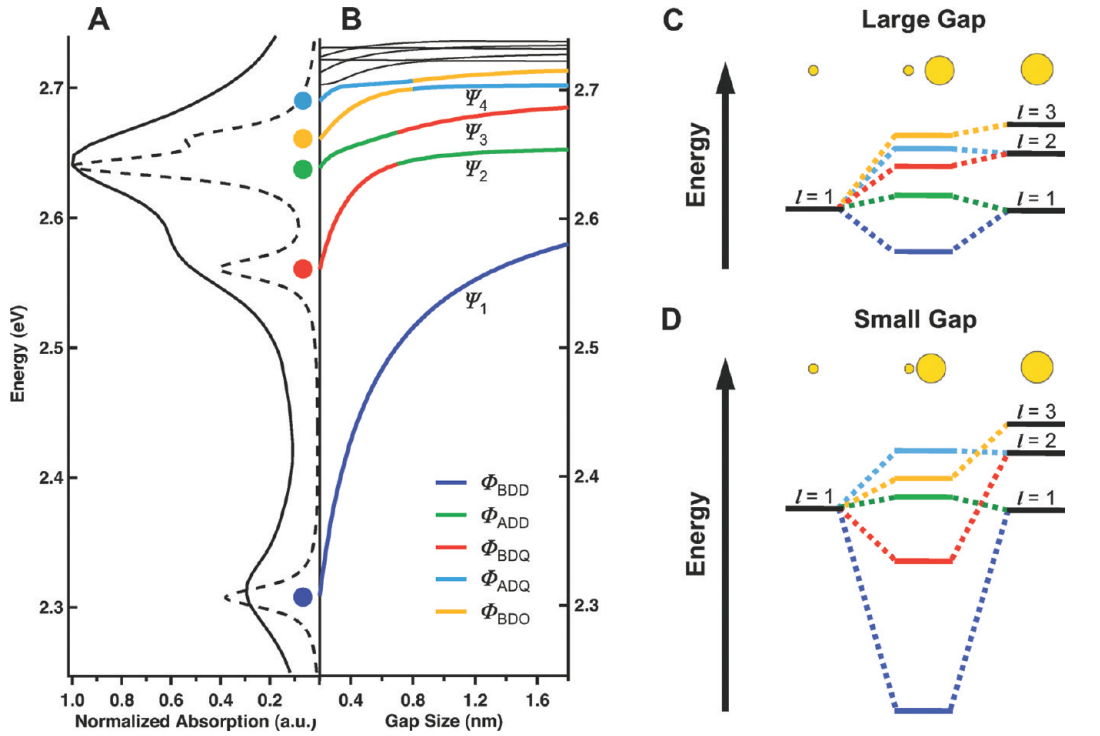

Figure 4. (A) Absorption spectra for heterodimer A with dimensions scaled down to 10% of the actual size, where the dimer is composed of spherical NPs with radii of 2.4 and 7.6 nm and a gap of 0.2 nm; (solid line) absorption calculated by FDTD using JC dielectric data; (dashed line) absorption calculated by the plasmon hybridization method using a Drude fit of the JC data with an artificially small damping parameter of $\delta = 0.01$ eV. Plasmon modes are identified as follows: bonding dipole−dipole (Φ_{BDD}, dark blue), antibonding dipole−dipole (Φ_{ADD}, green), bonding dipole−quadrupole (Φ_{BDQ}, red), antibonding dipole−quadrupole (Φ_{ADQ}, light blue), and bonding dipole−octupole (Φ_{BDO}, yellow). (B) Energies of the adiabatic plasmon modes of heterodimer A as a function of interparticle gap size. Avoided crossing behavior between modes Ψ_2 and Ψ_3 and between Ψ_4 and Ψ_5 are apparent. Plasmon hybridization diagrams for large (C) and small (D) gap sizes. In these diagrams, the dipolar energies of nanoparticles 1 and 2 are the same because the particles are in the quasistatic limit.

tral location at or near 600 nm. Because of the strong similarity among these spectra, a more detailed analysis of the plasmonic properties of heterodimer A will provide the essential information to describe the plasmon mode behavior in all of these structures.

Plasmon Modes of Heterodimer A: Heterodimer A consists of two adjacent Au nanospheres with one nanosphere (nanoparticle 1) significantly smaller than the other (nanoparticle 2). This size asymmetry provides the essential physical mechanism for plasmon hybridization in these structures: the dipole plasmon of the much smaller nanoparticle can couple efficiently to both the dipole and higher multipolar plasmons of the larger nanoparticle.

To obtain accurate mode assignments for heterodimer A, a systematic comparison must be performed between the experimentally observed spectral features and the hybridized plasmon modes of the heterodimer in the quasistatic limit. This is because plasmon hybridization theory, necessary for rigorous mode assignments, only applies to nanostructures in the quasistatic limit. This comparison is accomplished by first obtaining FDTD simulations of the heterodimer spectra that agree quantitatively with the experimentally obtained spectra, then by scaling down the nanoparticle sizes in the FDTD simulations to the quasistatic limit. The scaled-down FDTD simulations then agree quantitatively with the plasmon hybridization model and enable accurate mode assignments. Good agreement between FDTD simulations and experimental data has already been shown in Figure 3. To simplify our analysis for the identification of plasmon modes, we will adjust the geometry of heterodimer A from that reported in Table 1 to a dimer composed of two spherical NPs with radii of 24 and 76 nm and a gap size of 2 nm. To simulate this structure in the quasistatic regime, we reduce its dimensions by 90%, such that the particles have radii of 2.4 and 7.6 nm and a gap size of 0.2 nm. In Figure 4A, we compare the absorption spectrum of this reduced geometry calculated by FDTD (solid line) with that calculated by the plasmon hybridization method (dashed line), where we have used an artificially small damping parameter to more easily identify peak positions. Excellent agreement between these two approaches is obtained. This close correspondence enables us to rigorously identify the plasmon modes of heterodimer A.

In a homodimer, the inversion symmetry results in plasmon modes that can be classified as symmetric or antisymmetric. For longitudinal polarization, the symmetric modes are bonding modes and red shift with decreasing dimer separation; conversely, the antisymmet-

ric modes are antibonding modes and blue shift with decreasing dimer separation. Since the bonding and antibonding modes belong to different irreducible representations, the modes remain distinct for all interparticle separations and can cross each other. The lack of a mirror plane in a heterodimer reduces the symmetry of the overall structure and introduces coupling between all modes. To understand the plasmon modes responsible for the absorption spectrum of heterodimer A, we analyze the evolution of the plasmon modes with respect to interparticle separation, as shown in Figure 4B.

In this asymmetric dimer, the smaller nanoparticle 1 can couple to the dipolar and higher-energy multipolar modes of the larger nanoparticle 2. From low to high energy, the hybridized heterodimer modes that contribute to the spectrum are denoted $\Psi_1-\Psi_4$. Due to the reduced symmetry, the microscopic composition of some of these states will change with interparticle separation due to avoided crossings. We first consider the plasmon modes for large dimer separations. In this limit, hybridization is relatively weak, and the bonding and antibonding plasmon modes are formed as illustrated in Figure 4C. The modes are: (Φ_{BDD}) the bonding dipole−dipole (BDD) mode, resulting from symmetric hybridization between the dipolar plasmon of nanoparticle 1 with the dipolar plasmon of nanoparticle 2 (dark blue); (Φ_{ADD}) the antibonding dipole−dipole (ADD) mode, resulting from asymmetric hybridization between the dipolar plasmon of nanoparticle 1 with the dipolar plasmon of nanoparticle 2 (green); (Φ_{BDQ}) the bonding dipole−quadrupole (BDQ) mode, resulting from symmetric hybridization between the dipolar plasmon of nanoparticle 1 with the quadrupolar plasmon of nanoparticle 2 (red); (Φ_{ADQ}) the antibonding dipole−quadrupole (ADQ) mode, resulting from the asymmetric hybridization between the dipolar plasmon of nanoparticle 1 with the quadrupolar plasmon of nanoparticle 2 (light blue); (Φ_{BDO}) the bonding dipole−octupole mode (BDO), resulting from the symmetric hybridization between the dipolar plasmon of nanoparticle 1 with the octupolar plasmon of nanoparticle 2 (yellow).

In Figure 4B,D, we see how the hybridized plasmon modes of the heterodimer are modified as the distance between the two nanoparticles is decreased. The gap-dependent interactions between modes determine the energy of the hybridized modes in the intact heterodimer. This behavior is quite complex: in particular, we see that several of the antibonding plasmon modes exhibit avoided crossings with the bonding modes. A more detailed analysis of the eigenstates is necessary to interpret the exchange between plasmon mode amplitudes that gives rise to this behavior.

Because the modes interact very strongly, the Hamiltonian matrix for this system is not diagonal. In the present plasmon picture, each adiabatic plasmon mode (eigenvector) can be represented as a linear combination of the diabatic plasmon modes:[50]

$$|\Psi_n\rangle = C^n_{BDD}|\Phi_{BDD}\rangle + C^n_{ADD}|\Phi_{ADD}\rangle + C^n_{BDQ}|\Phi_{BDQ}\rangle + C^n_{ADQ}|\Phi_{ADQ}\rangle + C^n_{BDO}|\Phi_{BDO}\rangle \quad (1)$$

where C_i are the separation-dependent expansion coefficients of the Φ_i modes. The adiabatic energy trajectories shown in Figure 4B correspond to linear combinations of the plasmon eigenvectors, each denoted by a different color. The avoided crossing behavior observed in this calculation arises due to the strong dependence the coefficients of these modes have on interparticle separation.

In Figure 5, the avoided crossing that occurs between Ψ_2 and Ψ_3 seen in Figure 4B is examined in greater detail. In Figure 5A, the adiabatic states Ψ_2 and Ψ_3 and dashed green and red curves with approximate

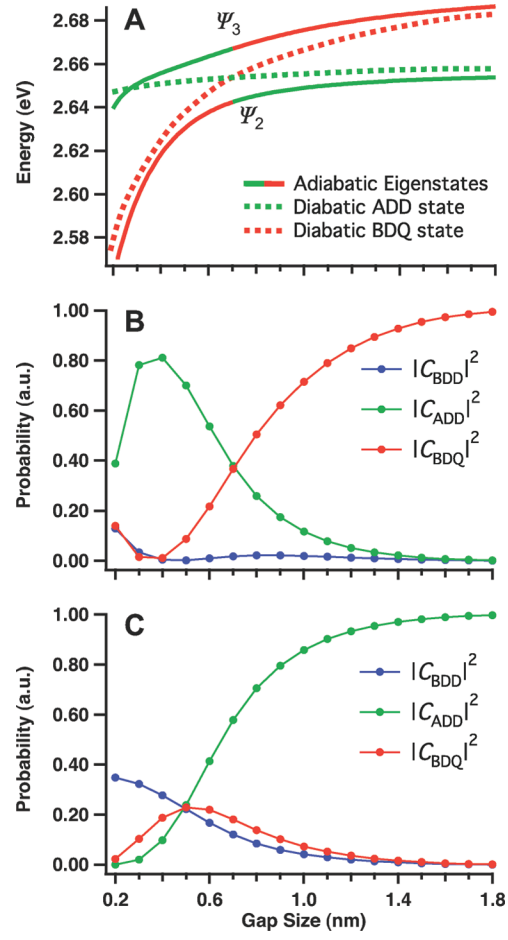

Figure 5. Avoided crossing between plasmon modes of heterodimer A. (A) Solid curves are the adiabatic eigenstates Ψ_2 and Ψ_3 with respect to gap size, as plotted in Figure 4B. Dotted curves are the diabatic Φ_{ADD} (green) and Φ_{BDQ} (red) states. (B) $|C_{BDD}|^2$ (blue), $|C_{ADD}|^2$ (green), and $|C_{BDQ}|^2$ (red) calculated by the plasmon hybridization method for Ψ_3. $|C_{ADD}|^2$ decreases at small gap sizes due to contributions from $|C_{BDD}|^2$, $|C_{BDQ}|^2$, and higher-order modes not shown. (C) Same coefficients in (B) calculated for Ψ_2. $|C_{BDQ}|^2$ decreases at small gap sizes in (C) due to contributions from $|C_{BDD}|^2$ and higher-order modes not shown.

values corresponding to the diabatic Φ_{ADD} and Φ_{BDQ} modes, respectively, are shown. At small gap sizes, Ψ_3 has less energy than the Φ_{ADD} mode because it also interacts with higher modes. Figure 5B gives the squares of the expansion coefficients C_i for Ψ_3. For large gap sizes, $|C_{BDQ}|^2$ is equal to 0.9996, and $|C_{BDD}|^2$ and $|C_{ADD}|^2$ are almost zero. As the nanoparticles approach each other, Ψ_3 gradually transitions from the Φ_{BDQ} mode to the Φ_{ADD} mode with a crossover point at a gap of 0.7 nm. When the gap reaches 0.4 nm, $|C_{ADD}|^2$ begins to decrease due to contributions from $|C_{BDD}|^2$, $|C_{BDQ}|^2$, and other higher-order modes. At 0.2 nm, $|C_{ADD}|^2$ is still the largest, with a value of 0.39. These data give clear evidence that the peak at 2.64 eV in Figure 4A corresponds to the Φ_{ADD} mode. The sum of these probabilities does not equal 1.0 because the remaining ~35% is attributable to other terms in the linear combination that are not shown.

The amplitudes C_i for the diabatic modes contributing to Ψ_2 are given in Figure 5C. At large separations, $|C_{ADD}|^2$ dominates with a value of 0.9996, and $|C_{BDQ}|^2$ is almost zero. With decreasing gap size, the modes begin to mix, resulting in a decrease of $|C_{ADD}|^2$ and an increase of $|C_{BDQ}|^2$. Unlike the case for Ψ_3, $|C_{BDD}|^2$ also becomes larger because the Φ_{BDD} mode experiences significant coupling with the Φ_{BDQ} mode. At about 0.5 nm, the contributions from Φ_{BDD}, Φ_{ADD}, and Φ_{BDQ} are similar in magnitude, and for smaller separations, the Φ_{BDD} mode begins to dominate Ψ_2. At 0.2 nm, $|C_{BDQ}|^2$ has a value of 0.023, which is much greater than that for $|C_{ADD}|^2$ at 1.97×10^{-5}. Therefore, we can assign the peak at 2.56 eV in Figure 4C to the Φ_{BDQ} mode. These observations illustrate the true implications of nonspherical symmetry in plasmonic systems, where each energy level is in fact an extended mixture of many different hybridized modes rather than a single hybridized mode. Further evidence of this is seen in Supporting Information Figure S4, which shows the probabilities of all five modes (Φ_{BDD}, Φ_{ADD}, Φ_{BDQ}, Φ_{ADQ}, and Φ_{BDO}) in the first four adiabatic eigenstates. For simplicity, however, we assign Ψ_2 to the Φ_{BDQ} mode and Ψ_1 to the Φ_{BDD} mode because, in Ψ_1, $|C_{BDD}|^2$ has the greatest contribution at all gap distances (Figure S4).

Similar avoided crossings exist for the higher-order adiabatic eigenstates. As the states become closer at higher energies, they experience increasingly complex avoided crossings, where many exchanges between plasmon modes can occur for a single eigenstate. For example, in addition to the exchange of modes already indicated between Ψ_4 and Ψ_5, closer inspection of Figure 4B reveals that Ψ_5 undergoes an additional avoided crossing with Ψ_6 at a gap of 0.3 nm. Similarly, Ψ_4 undergoes additional interactions with Ψ_3 at 0.3 nm, which is why Ψ_3 decreases in energy below the diabatic Φ_{ADD} state indicated in Figure 5A.

An understanding of these mode assignments allows us to better interpret the relative peak amplitudes in the spectrum in Figure 4A. In the quasistatic limit, the peak amplitudes are proportional to the strength with which each mode couples to the incident light field, which is in turn determined by the square of the overall dipole moment of that mode. One would expect the Ψ_1 mode to have the highest intensity. However, in the plasmon hybridization spectrum, the Ψ_3 mode is the most intense, followed by the Ψ_2 and Ψ_1 modes, with the Ψ_2 mode having a slightly higher intensity than the Ψ_1 mode. Although the Ψ_3 mode is primarily a combination of the dipole modes of nanoparticles 1 and 2, it also contains significant contributions from higher-order modes of nanoparticle 2, which enhance the strength of the overall dipole moment of the dimer for Ψ_3.

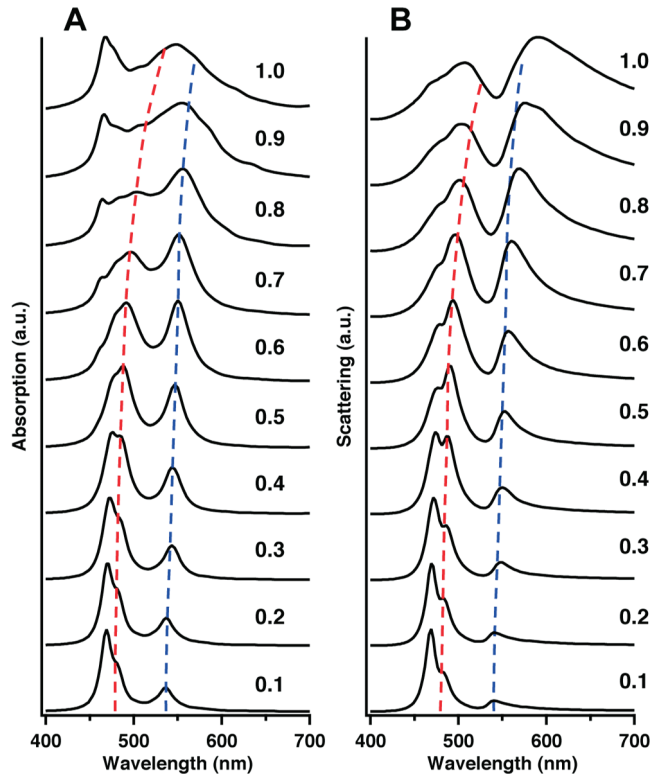

Figure 6. (A) Absorption and (B) scattering spectra calculated by FDTD for heterodimer A scaled to different sizes. The bottom spectra correspond to the quasistatic structure, which has spherical NPs with radii of 2.4 and 7.6 nm and a gap size of 0.2 nm. In each subsequent spectrum, the size is scaled up by a factor of 0.1 until the experimental size is reached, in which the dimer has NPs with radii of 24 and 76 nm and a gap size of 2 nm. Dashed lines indicate the red shifting of the Φ_{BDQ} (red) and Φ_{BDD} (blue) modes.

As can be seen from the properties of heterodimer A, which consists of a smaller nanosphere adjacent to a larger one, a size disparity between nanoparticles results in significantly more complex plasmon mixing behavior than in the case of a homodimer. For small gap sizes, the dipole mode in the smaller nanoparticle induces a localized charge on the larger nanoparticle (Supporting Information Figure S5). The overall charge distribution in the larger nanoparticle is therefore altered such that it is no longer purely dipolar in charac-

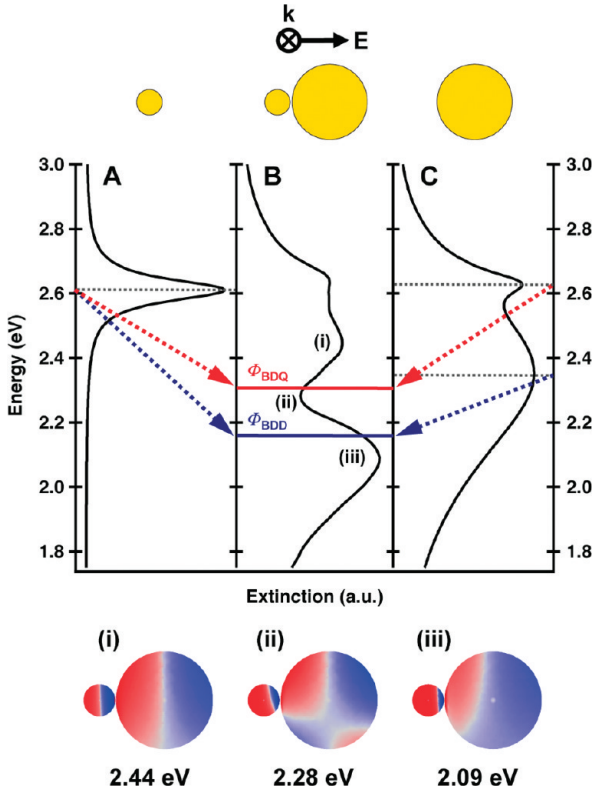

Figure 7. Plasmon hybridization diagram for heterodimer A, including extinction spectra of (A) a NP with a radius of 24 nm, (C) a NP with a radius of 76 nm, and (B) a dimer consisting of each of the nanoparticles in (A) and (C) with a gap of 2 nm. (A) and (C) were calculated with Mie theory using unpolarized incident light and the Drude model for the permittivity of Au. (B) was calculated by FDTD using longitudinally polarized light. Blue lines correspond to the Φ_{BDD} mode. Red lines correspond to the Φ_{BDQ} mode. (i–iii) Surface charge plot distributions of positive (red) and negative (blue) charge intensities calculated by the finite element method. The plot in (i) predominantly exhibits the Φ_{BDD} mode but also contains small, localized charge regions within the junction that are not visible in this figure (see Supporting Information Figure S5).

ter. As a result, higher-order modes in the larger nanoparticle couple more strongly to the dipole mode in the smaller nanoparticle. This is the physical mechanism behind the changes in the diabatic eigenstate probabilities (Figure 5B,C). Also, it means that contributions from higher-order hybridized modes in a given eigenstate actually increase the net dipole moment of the entire dimer structure, allowing it to couple more strongly to the incident light field. This is evident in the peak amplitudes of the modes in the quasistatic spectrum (Figure 4A).

Fano Resonance in Heterodimer A: With the plasmon modes of heterodimer A identified, we examine the plasmonic properties of the heterodimer A acquired in our experimental studies, where size-dependent phase retardation effects are very important. Our starting point is to rescale the size of the quasistatic geometry back to the experimental regime. Figure 6A,B gives a series of absorption and scattering spectra, respectively, for different sizes of heterodimer A, calculated by FDTD. The bottom spectrum in each panel corresponds to the quasistatic geometry previously introduced, and in each subsequent spectrum, the heterodimer dimensions are increased incrementally until the experimental dimensions (two nanospheres of radii 24 and 76 nm with an interparticle gap of 2 nm) are reached (top spectra).

As the dimensions of heterodimer A are increased, retardation effects cause all modes to shift to lower energies. The dashed blue and red lines in Figure 6A,B represent the spectral shifts of the Φ_{BDD} and Φ_{BDQ} modes, respectively. With increasing heterodimer size, the Φ_{BDQ} mode red shifts to a greater extent than the Φ_{BDD} mode. In the full-size structure, the Φ_{BDQ} mode overlaps the Φ_{BDD} mode in energy sufficiently to produce a Fano resonance, indicated by a dip in the scattering spectrum.

Figure 7 illustrates how the hybridization of the Φ_{BDD} and Φ_{BDQ} modes gives rise to the Fano resonance of heterodimer A in greater detail, by comparing the spectra of the individual constituent nanoparticles with the spectrum of heterodimer A. Panels A and C show the dipole resonances of nanoparticles 1 and 2 at 2.61 and 2.35 eV, respectively; the quadrupole resonance of nanoparticle 2 is at 2.63 eV. When the interparticle gap is 2 nm (Figure 7B), the plasmon modes hybridize and red shift in energy. The dipole resonances hybridize into the Φ_{BDD} mode (blue), and the dipole of nanoparticle 1 and the quadrupole of nanoparticle 2 hybridize into the Φ_{BDQ} mode (red). The Φ_{BDD} and Φ_{BDQ} modes couple strongly to each other in the quasistatic limit (Figure 5C). In the full-size structure (Figure 7B), the energy shifts of these modes due to phase retardation cause an increasing energy overlap, allowing them to couple to an even greater extent, resulting in a Fano resonance.

Surface charge plots of heterodimer A at 2.44, 2.28, and 2.09 eV provide a local field picture of the Fano resonance (Figure 7i–iii). The charge distributions at 2.44 and 2.09 eV are consistent with the Φ_{BDD} mode. However, in the spectral minimum at 2.28 eV, nanoparticle 1 exhibits a dipolar pattern while nanoparticle 2 exhibits a quadrupolar pattern. This charge distribution corresponds to the Φ_{BDQ} mode. This provides strong local evidence that the Φ_{BDQ} mode is narrow in comparison to the Φ_{BDD} mode, and that the coupling between these two modes is what gives rise to the Fano resonance.

Plasmon Modes of Heterodimers B–F: Following the identification of the plasmon modes in heterodimer A, similar mode assignments can be made for heterodimers B–F. The plasmon hybridization schemes for heterodimers B and C are comparable to the scheme of heterodimer A, except that, as the size of nanoparticle 1 increases, the Φ_{BDD} mode red shifts and the Φ_{BDQ} mode retains its location (Figure 3). This occurs due to changes in the amount of coupling between the modes of the individual nanoparticles. The progressively larger cross sec-

tion of nanoparticle 1 results in a larger dipole moment closer in energy to that of nanoparticle 2. Therefore, stronger coupling exists between the dipole modes of the constituent particles, causing a red shift in the Φ_{BDD} mode. However, now the coupling between the dipole mode of nanoparticle 1 and the quadrupole mode of nanoparticle 2 is weaker because these modes are further apart in energy. This should cause the Φ_{BDQ} mode to blue shift but does not because it is balanced by the red-shifted dipole mode of the larger size nanoparticle 1.

A similar argument can be made when comparing the scattering spectra of heterodimers A−C to those of heterodimers D−F (Figure 3). These spectra are virtually the same because plasmon coupling occurs primarily at the surfaces of the nanoparticles, and when nanoparticle 2 is a nanoshell, the effective plasmon coupling weakens due to the differences in energy of the plasmon resonances of the two nanoparticles. This should cause a blue shift in the Φ_{BDD} and Φ_{BDQ} modes, but it does not because it is balanced by the initially lower energy of the dipole resonance of the nanoshell. As a result, the Φ_{BDD} and Φ_{BDQ} modes in heterodimers D−F have nearly the same energy as those in heterodimers A−C.

Fano Resonances in Heterodimers B−F: Because the plasmon hybridization schemes for all heterodimers are quite similar, they all support Fano resonances similar to the one described for heterodimer A. As with heterodimer A, both peaks in the scattering spectrum correspond to the Φ_{BDD} mode, and the dip corresponds to the Φ_{BDQ} mode (Supporting Information Figure S6). However, when the size of nanoparticle 1 is increased and the Φ_{BDD} mode is red-shifted, the two modes overlap less and the Fano resonance weakens. Replacing the solid nanoparticle in dimers A−C with a nanoshell in dimers D−F does not significantly alter the Fano resonance because the plasmon energies of the corresponding structures are nearly equal.

Dimer C is unique in that it is a homodimer with a Fano resonance, while the rest of the structures are heterodimers. The presence of a Fano resonance in the spectrum of this structure shows that strong asymmetry is not always necessary to produce a Fano resonance in a plasmonic nanostructure. Here, Fano resonances are possible simply because dark modes of higher multipolar composition overlap with the bright continuum of the Φ_{BDD} mode.[6] The nanoparticles do not need to have different sizes for this to occur. Therefore, other plasmonic homodimers consisting of spherical nanoparticles are expected to exhibit Fano resonances, as long as the bright Φ_{BDD} and dark Φ_{BDQ} modes overlap sufficiently in energy. For example, nanoshell homodimers that were recently studied[13] also show this behavior. Although the nanoshells were slightly smaller than those used in the present study, the spectrum for longitudinal excitation of the strongly interacting dimer was strikingly similar to the spectra for dimers C and F in Figure 3. It is therefore quite likely that the spectra of the nanoshell dimers previously reported contain Fano resonances (we have included surface charge plots of nanoshell dimers that support this claim; see Figure S6 in the Supporting Information).

We have seen here that, although the experimental geometries in Figure 2 show deviations from ideal shapes, the theoretical fitting and assignment of plasmon modes is possible. In an arbitrarily selected dimer, typical abnormalities in the geometry of the individual particles might include rough surfaces, facets, or prolate shapes. For incident polarization in the longitudinal direction, such deviations will affect the scattering spectra primarily when they are in the junction region of the dimer or along the dimer axis. In our experiment, the particles had sufficiently spheroidal shapes that an adequate theoretical fitting and assignment of modes could be performed satisfactorily.

Transverse Excitation of Heterodimers. Excitation of plasmonic dimers with polarization transverse to the interparticle axis has received far less attention than the case of longitudinal excitation because the field enhancement and plasmon coupling are far weaker for this case. In heterodimers composed of a solid Au nanosphere (NP) and a Au nanoshell (NS), however, polarization in the transverse direction gives rise to a striking asymmetry in the scattering properties, depending on the direction of propagation of incident light.

Experimental and theoretical scattering spectra of heterodimers A−F for transversely polarized incident light are shown in Figure 8. Conditions for all spectra are the same as those used to obtain the data in Figure 3, except the angle of polarization is now perpendicular to the dimer axis and parallel to the substrate with the k-vector parallel to the dimer axis.

Heterodimers A−C have similar spectra, with a single prominent peak appearing at nominally 600 nm. This feature for heterodimer A is slightly red-shifted and broader than for heterodimers B and C. This appears to be because nanoparticle 2 in heterodimer A is prolate with a larger radius in the transverse direction. Heterodimers D−F have spectral features that are red-shifted relative to the spectra of heterodimers A−C due to the initially lower energy of the NS resonance. Also, heterodimers D−F have noticeably different spectra with increasing nanoparticle 1 size, particularly when light is directed onto nanoparticle 1 first (green curves).

Transverse Excitation of Heterodimer F: This asymmetric scattering behavior may be understood by examining heterodimer F in detail since this heterodimer shows the most prominent asymmetry of the heterodimers studied. With transverse excitation, plasmon coupling is relatively weak, and therefore, the hybridized modes have nearly the same energies as the modes of the constituent nanoparticles (Figure 9A). In heterodimer F,

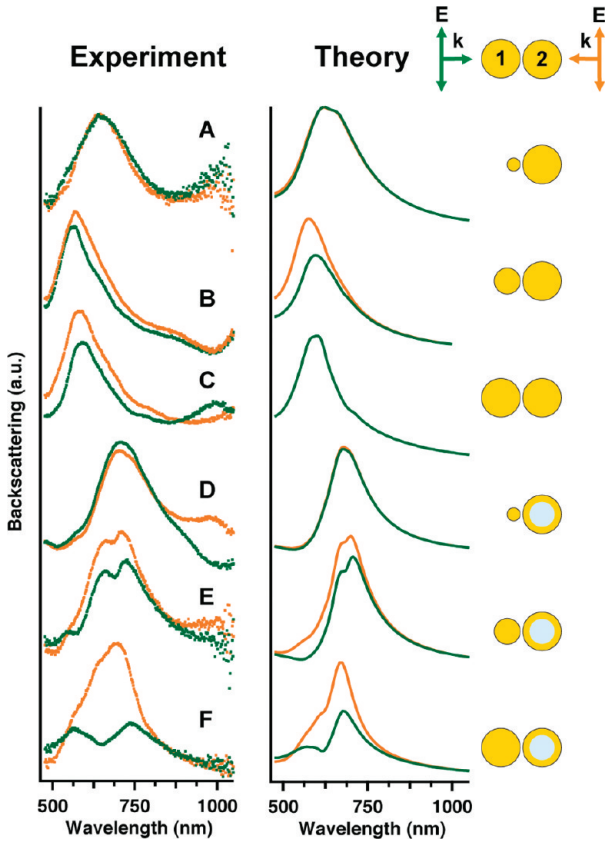

Figure 8. Experimental and theoretical scattering spectra (calculated by FDTD) for heterodimers A−F with transversely polarized incident light. The theoretical spectrum for heterodimer C includes only one direction of propagation due to the symmetry of the structure. The theoretical spectra for opposing k-vectors in heterodimers A and D are nearly identical.

the higher-energy mode is closer to the dipolar resonance of the NP and the lower-energy mode is closer to the dipolar resonance of the NS. These modes are the transverse symmetric (Φ_{TS}) and transverse antisymmetric (Φ_{TA}) dipole resonances, respectively.

Using the plasmon hybridization method, we can mathematically express the dipolar part of the Φ_{TS} and Φ_{TA} modes as linear combinations of the dipolar resonances of the nanoparticle (ϕ_{NP}) and the nanoshell (ϕ_{NS}):

$$|\Phi_{TS}\rangle = \zeta|\phi_{NP}\rangle + \sqrt{(1-\zeta^2)}|\phi_{NS}\rangle \quad (2)$$

$$|\Phi_{TA}\rangle = -\sqrt{(1-\zeta^2)}|\phi_{NP}\rangle + \zeta|\phi_{NS}\rangle \quad (3)$$

where ζ is a constant that depends on the relative energies of the NP and NS modes and their interaction strength. In these expansions, the ϕ_{NP}, ϕ_{NS}, Φ_{TS}, and Φ_{TA} modes are orthonormal. Given that the Φ_{TS} mode is closest in energy to the ϕ_{NP} mode, we can conclude that ϕ_{NP} will have a significantly larger contribution than ϕ_{NS} to the Φ_{TS} mode. Similarly, ϕ_{NS} will have a larger contribution than ϕ_{NP} to the Φ_{TA} mode. In eqs 2 and 3, this condition is satisfied when $\zeta \gg (1-\zeta^2)^{1/2}$.

The asymmetric scattering behavior of the heterodimer is caused by retardation effects, that is, the finite speed of light. To understand the dependence of the scattering spectra of the direction of excitation, we generalize the argument put forward in an application to metallic nanorings.[51] For light incident from the left where the incident light front first encounters the NP, only the NP will be polarized (Figure 9B). The instantaneous polarization of the NP is equivalent to a superposition of both the Φ_{TS} and Φ_{TA} modes. Since the Φ_{TS} is more NP-like, left-handed incidence will result in a stronger excitation of Φ_{TS}. This can be seen in the E-field enhancement shown in Figure 9D, calculated for 571 nm, the wavelength of excitation of the Φ_{TS} mode. The nanoparticle, on the left side of the figure, clearly has a greater enhancement at its surface, indicating that it is coupling more strongly to light than the nanoshell. In the opposite case, where the incident light first encounters the nanoshell, the instantaneous polarization of the NS (Figure 9C) results in a stronger excitation of the Φ_{TA} mode. Again, this is evident in the E-field plot (Figure 9E), where the nanoshell provides a higher near-field amplitude than the nanoparticle at 675 nm, the wavelength of excitation for the Φ_{TA} mode.

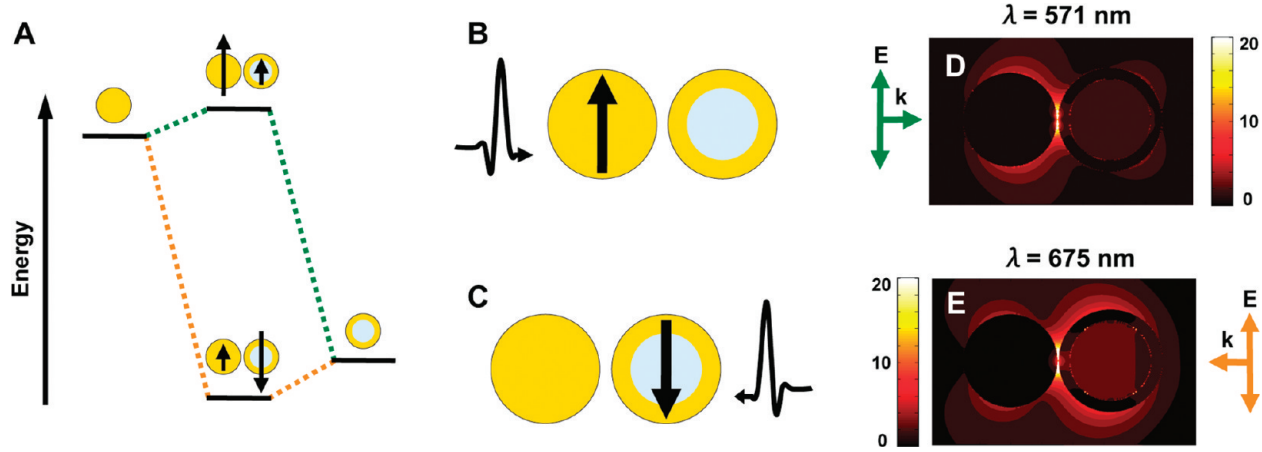

Figure 9. (A) Schematic plasmon hybridization diagram of heterodimer F. Schematic polarization of the dimer when transversely polarized incident light first encounters the NP (B) and NS (C). Electric field enhancement plots calculated by FDTD of the dimer when transversely polarized incident light first encounters the NP (D) and the NS (E) at λ = 571 and 675 nm, respectively.

These data suggest that, when a certain particle is excited more than the other, the corresponding hybridized mode is excited. We can examine this mathematically by rearranging eqs 2 and 3 to solve for the ϕ_{NP} and ϕ_{NS} modes:

$$|\phi_{NP}\rangle = \zeta|\Phi_{TS}\rangle - \left(\sqrt{1-\zeta^2}\right)|\Phi_{TA}\rangle \quad (4)$$

$$|\phi_{NS}\rangle = \left(\sqrt{1-\zeta^2}\right)|\Phi_{TS}\rangle + \zeta|\Phi_{TA}\rangle \quad (5)$$

These expressions clearly show that a transient polarization of the NP or the NS is equivalent to a coherent superposition of both the Φ_{TA} and Φ_{TS} modes. Using the condition that $\zeta \gg (1-\zeta^2)^{1/2}$, it is evident that a transient polarization of the NP is equivalent to a predominant excitation of the Φ_{TS} mode, while a transient polarization of the NS results in a predominant excitation of the Φ_{TA} mode.

A more detailed numerical investigation of the scattering properties of heterodimer F is presented in Figure 10. In panel A, we compare the scattering spectra of the dimer with the scattering spectra of the individual NP and NS under the same simulation conditions. When light incident on the heterodimer encounters the NS first, the Φ_{TA} mode has a much higher intensity than the higher-energy Φ_{TS} mode, which appears as a weak shoulder. However, when the excitation direction is reversed and light incident on the heterodimer encounters the NP first, both modes decrease in intensity, and the Φ_{TS} mode is somewhat more prominent. These numerical findings are in excellent agreement with the qualitative picture according to eqs 2 and 4.

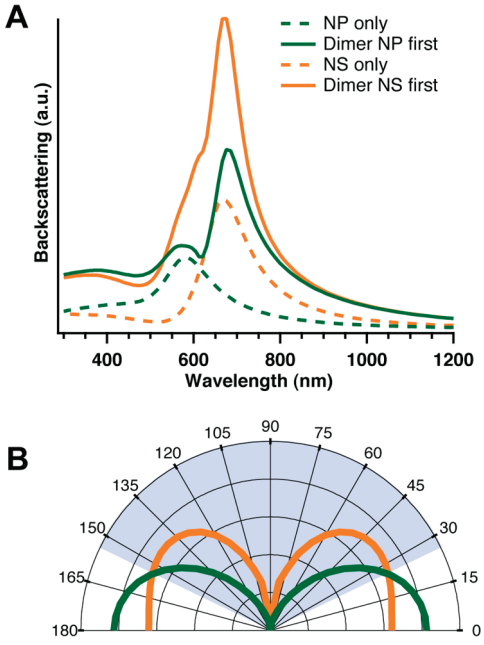

Figure 10. (A) Theoretical scattering spectra of a NP with a radius of 75 nm (dashed green), a NS with an inner radius of 66 nm and an outer radius of 84 nm (dashed yellow), heterodimer F with transversely polarized incident light incident on the NP first (solid green), and heterodimer F with transversely polarized incident light incident on the NS first (solid yellow). (B) Scattering distribution of heterodimer F with transversely polarized incident light incident on the NP first (green) and the NS first (yellow). The blue shaded region represents the solid angle corresponding to collection of scattered light from the structure. Both distributions in (B) are for λ = 675 nm light. All calculations were performed using three-dimensional finite difference time domain (FDTD) simulations.

The angular distribution of the scattered light depends on which hybridized mode is excited and thus on to the direction of heterodimer excitation. The scattering distributions for light of wavelength 675 nm incident on the NS first (yellow) and on the NP first (green) are shown in Figure 10B. The shaded region between 26 and 154° represents the solid angle defined by the numerical aperture of the dark-field objective used to collect the experimental spectra. Since the cone angle encompasses a larger portion of the NS first case (yellow pattern) than the NP first case (green pattern), more light is collected in the case of NS first excitation, which agrees with our experimental observation that the scattering spectrum for the NS first case is significantly higher in intensity than the case of NP first excitation. Such a prominent dependence of the scattering behavior on the direction of incidence of light suggests potential application of these structures as photonic nanodiodes.

Transverse Excitation of Heterodimers A—E: The transverse excitation scattering properties of the heterodimer are primarily determined by the relative sizes of the scattering cross sections of each constituent nanoparticle. In heterodimer F, the NS has a larger scattering cross section than the NP (Figure 10A). In any dimer, if the scattering cross section of one nanoparticle is significantly larger than that of the adjacent nanoparticle, then the larger nanoparticle will dominate the scattering properties regardless of which nanoparticle gets excited first. For example, heterodimer F has the most noticeable difference in scattering spectra (Figure 8). Heterodimer E, however, has only a slight asymmetry, and heterodimer D has virtually no asymmetry at all. For heterodimer D, the NS dominates the scattering properties of the dimer. In this case, the much smaller NP has no effect on the scattering properties of the much larger NS. Heterodimer E has a slight scattering asymmetry because the scattering cross section of the NP is large enough to have an effect on the overall scattering properties of the heterodimer. This effect is even greater in heterodimer F, where the scattering cross section of the NP is even larger.

Heterodimers A, B, and C exhibit only a very small scattering asymmetry depending on the direction of incident excitation (Figure 8). In these three cases, both nanoparticles are solid nanospheres, and the dipolar plasmons of the constituent nanoparticles are extremely close in energy for transversely polarized excitation. In these cases, the symmetric and antisymmetric modes have a much smaller difference in energy than for longitudinal polarization excitation, and they

cannot be distinguished in the scattering spectra. We do observe in heterodimers B and C, however, that the overall scattering distribution does change shape when the two nanospheres become more equal in size. Although heterodimer C was simulated as a homodimer, resulting in identical theoretical spectra, deviations in the experimental geometry caused asymmetric scattering profiles (Figure 8). We speculate that when nanoparticle 2 is excited first, the scattering intensity is larger because the particle is slightly prolate (Figure 2C).

SUMMARY

Individual plasmonic heterodimers assembled by an electrostatic surface migration method have been studied using polarization-dependent dark-field microspectroscopy. Analyzing our experimental observations of these structures using a combination of plasmon hybridization and FDTD, we are able to provide a universal picture for understanding several of the unique optical properties of these structures. Avoided crossing behavior, Fano resonances, and asymmetric scattering of heterodimer structures are all examined, and the dependence of nanoparticle size and resonant energy to these effects has been studied in detail. It is remarkable that such a simple structure, consisting of two adjacent metallic nanoparticles of mismatched size and resonant energy, gives rise to this range of properties. As studies of plasmonic structures extend to more complex geometries, it is likely that these, or analogous, effects will be observable.

METHODS

Dimer Synthesis. Au nanoparticles (NPs) and nanoshells (NSs) were prepared as described in the text. Centrifugation speeds and final concentrations of all NP suspensions are given in Supporting Information Table S1. Extinction spectra of NP and NS solutions were obtained by a Varian Cary 5000 UV−Vis−NIR spectrometer (Figure S2A). For the synthesis of heterodimers A, B, D, E, and F, appropriate combinations of NP and NS suspensions were combined in 1:1 volumetric ratios. NP−NP homodimers (dimer C) were prepared with a rinsed suspension of NPs with radii of 75 nm.

Glass coverslips coated with (3-aminopropyl)triethoxysilane (APTES, Sigma Aldrich) served as substrates for the surface migration of NPs and NSs. Coverslips with dimensions of 22 × 22 mm with 1.5 thickness (Fisher) were cleaned by oxygen plasma for 1.5 min and placed in an ethanolic solution of 10% v/v APTES for 30 min. Then they were rinsed and sonicated in 200 proof ethanol for 5 min in a Teflon coverslip minirack (Invitrogen). Rinsing and sonication was repeated four times. Thorough cleaning of APTES-functionalized substrates is important for removing multilayers of APTES, which can cause aggregation of particles upon deposition.

To ensure proper cross-linking of the APTES monolayer, the coverslips were laid flat in a glass dish and annealed at 120 °C for 30 min. The substrates were cooled to room temperature and placed in the particle suspensions for 2 h. Then they were quickly rinsed with ethanol and placed in an ethanolic solution of 1 mM 11-mercaptoundecanol (MUOH) overnight, during which time the particles underwent surface migration to form dimers. The substrates were rinsed with ethanol, let dry in a fume hood, and sonicated one-by-one in 5 mL of deionized water, resulting in very stable dimer suspensions. The particles/mL concentration of each suspension increased as more substrates were sonicated (Figure S2B). After the desired concentration was reached, the solutions were stored in sealed containers at room temperature. These suspensions remained stable for more than 8 months, requiring 10 min of sonication or less to redistribute the particles (Figure S2C).

Analysis of individual dimer structures by dark-field scattering was possible by mounting the dimers on glass substrates. Fresh glass coverslips were cleaned with oxygen plasma for 1.5 min and placed in an ethanolic solution of 0.01 wt % poly(4-vinyl pyridine) overnight. Then they were rinsed with ethanol and dried with nitrogen gas. Indexed grids designed for transmission electron microscopy were attached to the substrates to serve as stencils to prepare alignment markings. An electron beam evaporator was used to evaporate a 2 nm adhesion layer of Ti, followed by a 20 nm layer of Au. The grids were removed, and a few drops of the fresh dimer suspensions were placed on the substrates for 15 min to 3 h. The coverslips were lightly rinsed with deionized water and dried in air in a fume hood. This resulted in substrate-bound dimers spaced far apart for adequate spectroscopic analysis without interference from neighboring particles.

Dark-Field Microspectroscopy. The instrumentation for spectroscopic analyses of dimers was identical to that reported previously.[13] Briefly, the sample was placed on a rotatable stage on a Zeiss Axiovert 200 MAT inverted optical microscope equipped with a 100× dark-field objective with a numerical aperture of 0.9 (Zeiss). A halogen lamp served as a white light source. A linear polarizing filter (LPVIS 100, Thorlabs) was placed in the incident light path and rotated appropriately for s-polarization. To maintain s-polarized light at the sample plane, an aluminum disk with a small wedge-shaped cutout was placed next to the polarizing filter in order to block certain parts of the beam that would otherwise reflect off of an annular mirror to result in mixed polarization. This configuration ensured not only a fixed polarization angle with respect to the substrate but also a fixed direction of incidence. Therefore, the polarization angle and direction of incidence with respect to individual dimers could be adjusted by rotating the sample itself. Spectroscopic data were collected with an Acton Microspec 2150i spectrometer attached to a thermoelectrically cooled CCD camera (Princeton Instruments PhotonMax 512).

FEM Simulations. Surface charge plots of the dimers were obtained by COMSOL Multiphysics, a commercial software that uses the finite element method (FEM). The geometries of the simulations were identical to those used in FDTD with the exception of all dielectric materials, including the MUOH passivation layer, the PVP layer, and the substrate. These were removed to avoid computational difficulties due to small mesh elements. Although the absorption and scattering spectra were blue-shifted from those in the FDTD simulations, hybridization between plasmon modes was the same. Therefore, charge plots were selected at the appropriate wavelengths corresponding to those in the FDTD simulations (Figure S6).

Acknowledgment. We gratefully acknowledge Kui Bao, Britain Willingham, Nikolay Mirin, Mark Knight, Surbhi Lal, and Liane Slaughter for helpful discussions. We also thank Jason Hafner for use of the dark-field microspectrometer and Joseph Young for nanoshell synthesis. This material is based upon work supported as part of the Center for Advanced Solar Photophysics, an Energy Frontier Research Center funded by the U.S. Department of Energy, Office of Science, Office of Basic Energy Sciences. This work was supported by the DoD NSSEFF, the Air Force Office of Scientific Research (F49620-03-C-0068), the Robert A. Welch Foundation (C-1220 and C1222), the Multidisciplinary University Research Initiative (MURI) W911NF-04-01-0203, the NSF IGERT Fellowship (L.V.B. and B.L.), and the Shared University Grid at Rice (SUG@R) team.

Supporting Information Available: Scanning electron microscopy images and further discussion of electrostatic surface migration; experimental parameters for dimer synthesis; ensemble extinction spectra of nanoparticles and nanoshells and suspensions of heterodimers; backscattering spectra of heterodimer A calculated by FDTD with different particle shapes and gap sizes; probability as a function of dimer gap size calculated by the plasmon hybridization method for diabatic plasmon eigenstates in the first four adiabatic states of heterodimer A; surface charge plots of heterodimer A calculated by FEM at different viewing angles; surface charge plots and accompanying extinction spectra of heterodimers A−F and nanoshell homodimers calculated by FEM with longitudinal excitation. This material is available free of charge via the Internet at http://pubs.acs.org.

REFERENCES AND NOTES

1. Kreibig, U.; Althoff, A.; Pressmann, H. Veiling of Optical Single-Particle Properties in Many-Particle Systems by Effective Medium and Clustering Effects. *Surf. Sci.* **1981**, *106*, 308–317.
2. Quinten, M.; Kreibig, U.; Schonauer, D.; Genzel, L. Opitcal-Absorption Spectra of Pairs of Small Metal Particles. *Surf. Sci.* **1985**, *156*, 741–750.
3. Rechberger, W.; Hohenau, A.; Leitner, A.; Krenn, J.; Lamprecht, B.; Aussenegg, F. Optical Properties of Two Interacting Gold Nanoparticles. *Opt. Commun.* **2003**, *220*, 137–141.
4. Su, K.; Wei, Q.; Zhang, X.; Mock, J.; Smith, D.; Schultz, S. Interparticle Coupling Effects on Plasmon Resonances of Nanogold Particles. *Nano Lett.* **2003**, *3*, 1087–1090.
5. Tabor, C.; Van Haute, D.; El-Sayed, M. A. Effect of Orientation on Plasmonic Coupling between Gold Nanorods. *ACS Nano* **2009**, *3*, 3670–3678.
6. Nordlander, P.; Oubre, C.; Prodan, E.; Li, K.; Stockman, M. Plasmon Hybridizaton in Nanoparticle Dimers. *Nano Lett.* **2004**, *4*, 899–903.
7. Funston, A. M.; Novo, C.; Davis, T. J.; Mulvaney, P. Plasmon Coupling of Gold Nanorods at Short Distances and in Different Geometries. *Nano Lett.* **2009**, *9*, 1651–1658.
8. Berthelot, J.; Bouhelier, A.; Huang, C.; Margueritat, J.; Colas-des-Francs, G.; Finot, E.; Weeber, J.-C.; Dereux, A.; Kostcheev, S.; El Ahrach, H. I.; Baudrion, A.-L.; Plain, J.; Bachelot, R.; Royer, P.; Wiederrecht, G. P. Tuning of an Optical Dimer Nanoantenna by Electrically Controlling Its Load Impedance. *Nano Lett.* **2009**, *9*, 3914–3921.
9. Camargo, P. H. C.; Rycenga, M.; Au, L.; Xia, Y. Isolating and Probing the Hot Spot Formed between Two Silver Nanocubes. *Angew. Chem., Int. Ed.* **2009**, *48*, 2180–2184.
10. Chen, H.; Sun, Z.; Ni, W.; Woo, K. C.; Lin, H.-Q.; Sun, L.; Yan, C.; Wang, J. Plasmon Coupling in Clusters Composed of Two-Dimensionally Ordered Gold Nanocubes. *Small* **2009**, *5*, 2111–2119.
11. Khoury, C. G.; Norton, S. J.; Vo-Dinh, T. Plasmonics of 3-D Nanoshell Dimers Using Multipole Expansion and Finite Element Method. *ACS Nano* **2009**, *3*, 2776–2788.
12. Kim, D.-S.; Heo, J.; Ahn, S.-H.; Han, S. W.; Yun, W. S.; Kim, Z. H. Real-Space Mapping of the Strongly Coupled Plasmons of Nanoparticle Dimers. *Nano Lett.* **2009**, *9*, 3619–3625.
13. Lassiter, J.; Aizpurua, J.; Hernandez, L.; Brandl, D.; Romero, I.; Lal, S.; Hafner, J.; Nordlander, P.; Halas, N. Close Encounters between Two Nanoshells. *Nano Lett.* **2008**, *8*, 1212–1218.
14. Liaw, J.-W.; Chen, J.-H.; Chen, C.-S.; Kuo, M.-K. Purcell Effect of Nanoshell Dimer on Single Molecule's Fluorescence. *Opt. Express* **2009**, *17*, 13532–13540.
15. Liu, M.; Lee, T.-W.; Gray, S. K.; Guyot-Sionnest, P.; Pelton, M. Excitation of Dark Plasmons in Metal Nanoparticles by a Localized Emitter. *Phys. Rev. Lett.* **2009**, *102*, 107401.
16. Marhaba, S.; Bachelier, G.; Bonnet, C.; Broyer, M.; Cottancin, E.; Grillet, N.; Lerme, J.; Vialle, J.-L.; Pellarin, M. Surface Plasmon Resonance of Single Gold Nanodimers near the Conductive Contact Limit. *J. Phys. Chem. C* **2009**, *113*, 4349–4356.
17. Oubre, C.; Nordlander, P. Finite-Difference Time-Domain Studies of the Optical Properties of Nanoshell Dimers. *J. Phys. Chem. B* **2005**, *109*, 10042–10051.
18. Pecharroman, C. Influence of the Close Sphere Interaction on the Surface Plasmon Resonance Absorption Peak. *Phys. Chem. Chem. Phys.* **2009**, *11*, 5922–5929.
19. Romero, I.; Aizpurua, J.; Bryant, G. W.; Garcia de Abajo, F. J. Plasmons in Nearly Touching Metallic Nanoparticles: Singular Response in the Limit of Touching Dimers. *Opt. Express* **2006**, *14*, 9988–9999.
20. Wu, D. J.; Cheng, Y.; Liu, X. J. Hot Spots" Induced Near-Field Enhancements in Au Nanoshell and Au Nanoshell Dimer. *Appl. Phys. B* **2009**, *97*, 497–503.
21. Yan, J.; Gao, S. Plasmon Resonances in Linear Atomic Chains: Free-Electron Behavior and Anisotropic Screening of d Electrons. *Phys. Rev. B* **2008**, *78*, 235413.
22. Zuloaga, J.; Prodan, E.; Nordlander, P. Quantum Description of the Plasmon Resonances of a Nanoparticle Dimer. *Nano Lett.* **2009**, *9*, 887–891.
23. Dadosh, T.; Sperling, J.; Bryant, G. W.; Breslow, R.; Shegai, T.; Dyshel, M.; Haran, G.; Bar-Joseph, I. Plasmonic Control of the Shape of the Raman Spectrum of a Single Molecule in a Silver Nanoparticle Dimer. *ACS Nano* **2009**, *3*, 1988–1994.
24. Dhawan, A.; Norton, S. J.; Gerhold, M. D.; Vo-Dinh, T. Comparison of FDTD Numerical Computations and Analytical Multipole Expansion Method for Plasmonics-Active Nanosphere Dimers. *Opt. Express* **2009**, *17*, 9688–9703.
25. Harris, N.; Arnold, M. D.; Blaber, M. G.; Ford, M. J. Plasmonic Resonances of Closely Coupled Gold Nanosphere Chains. *J. Phys. Chem. C* **2009**, *113*, 2784–2791.
26. Hossain, M. K.; Huang, G. G.; Kaneko, T.; Ozaki, Y. Surface-Enhanced Raman Scattering and Plasmon Excitations from Isolated and Elongated Gold Nanoaggregates. *Chem. Phys. Lett.* **2009**, *477*, 130–134.
27. Hossain, M. K.; Kitahama, Y.; Biju, V.; Itoh, T.; Kaneko, T.; Ozaki, Y. Surface Plasmon Excitation and Surface-Enhanced Raman Scattering Using Two-Dimensionally Close-Packed Gold Nanoparticles. *J. Phys. Chem. C* **2009**, *113*, 11689–11694.
28. Li, Z.; Shegai, T.; Haran, G.; Xu, H. Multiple-Particle Nanoantennas for Enormous Enhancement and Polarization Control of Light Emission. *ACS Nano* **2009**, *3*, 637–642.
29. Palomba, S.; Danckwerts, M.; Novotny, L. Nonlinear Plasmonics with Gold Nanoparticle Antennas. *J. Opt. A* **2009**, *11*, 114030.
30. Xu, H.; Bjerneld, E.; Kall, M.; Borjesson, L. Spectroscopy of Single Hemoglobin Molecules by Surface Enhanced Raman Scattering. *Phys. Rev. Lett.* **1999**, *83*, 4357–4360.
31. Zhang, W.; Fischer, H.; Schmid, T.; Zenobi, R.; Martin, O. J. F. Mode-Selective Surface-Enhanced Raman Spectroscopy Using Nanofabricated Plasmonic Dipole Antennas. *J. Phys. Chem. C* **2009**, *113*, 14672–14675.
32. Stockman, M.; Faleev, S.; Bergman, D. Localization *versus* Delocalization of Surface Plasmons in Nanosystems: Can One State Have Both Characteristics? *Phys. Rev. Lett.* **2001**, *87*, article no. 167401.
33. Liu, H.; Liu, Y. M.; Li, T.; Wang, S. M.; Zhu, S. N.; Zhang, X. Coupled Magnetic Plasmons in Metamaterials. *Phys. Status Solidi B* **2009**, *246*, 1397–1406.
34. Wang, H.; Wu, Y.; Lassiter, B.; Nehl, C. L.; Hafner, J. H.; Nordlander, P.; Halas, N. J. Symmetry Breaking in Individual Plasmonic Nanoparticles. *Proc. Natl. Acad. Sci. U.S.A.* **2006**, *103*, 10856–10860.
35. Chen, C.-Y.; Un, I.-W.; Tai, N.-H.; Yen, T.-J. Asymmetric Coupling between Subradiant and Superradiant Plasmonic Resonances and Its Enhanced Sensing Performance. *Opt. Express* **2009**, *17*, 15372–15380.
36. Fano, U. Effects of Configuration Interaction on Intensities and Phase Shifts. *Phys. Rev.* **1961**, *124*, 1866–1878.

37. Fofang, N. T.; Park, T.-H.; Neumann, O.; Mirin, N. A.; Nordlander, P.; Halas, N. J. Plexcitonic Nanoparticles: Plasmon-Exciton Coupling in Nanoshell-J-Aggregate Complexes. *Nano Lett.* **2008**, *8*, 3481–3487.
38. Liu, N.; Langguth, L.; Weiss, T.; Kaestel, J.; Fleischhauer, M.; Pfau, T.; Giessen, H. Plasmonic Analogue of Electromagnetically Induced Transparency at the Drude Damping Limit. *Nat. Mater.* **2009**, *8*, 758–762.
39. Liu, N. A.; Weiss, T.; Mesch, M.; Langguth, L.; Hirscher, U. E. M.; Sonnichsen, C.; Giessen, H. Planar Metamaterial Analogue of Electromagnetically Induced Transparency for Plasmonic Sensing. *Nano Lett.* **2009**, *9*, 1–4.
40. Maier, S. A. Waveguiding—The Best of Both Worlds. *Nat. Photonics* **2008**, *2*, 460–461.
41. Mirin, N. A.; Bao, K.; Nordlander, P. Fano Resonances in Plasmonic Nanoparticle Aggregates. *J. Phys. Chem. A* **2009**, *113*, 4028−4034.
42. Pakizeh, T.; Kall, M. Unidirectional Ultracompact Optical Nanoantennas. *Nano Lett.* **2009**, *9*, 2343–2349.
43. Prodan, E.; Nordlander, P. Plasmon Hybridization in Spherical Nanoparticles. *J. Chem. Phys.* **2004**, *120*, 5444–5454.
44. Prodan, E.; Radloff, C.; Halas, N.; Nordlander, P. A Hybridization Model for the Plasmon Response of Complex Nanostructures. *Science* **2003**, *302*, 419–422.
45. Brinson, B. E.; Lassiter, J. B.; Levin, C. S.; Bardhan, R.; Mirin, N.; Halas, N. J. Nanoshells Made Easy: Improving Au Layer Growth on Nanoparticle Surfaces. *Langmuir* **2008**, *24*, 14166–14171.
46. Oldenburg, S.; Averitt, R.; Westcott, S.; Halas, N. Nanoengineering of Optical Resonances. *Chem. Phys. Lett.* **1998**, *288*, 243–247.
47. Johnson, P. B.; Christy, R. W. Optical Constants of the Noble Metals. *Phys. Rev. B* **1972**, *6*, 4370–4379.
48. Knight, M. W.; Wu, Y.; Lassiter, J. B.; Nordlander, P.; Halas, N. J. Substrates Matter: Influence of an Adjacent Dielectric on an Individual Plasmonic Nanoparticle. *Nano Lett.* **2009**, *9*, 2188–2192.
49. Ye, J.; Van Dorpe, P.; Lagae, L.; Maes, G.; Borghs, G. Observation of Plasmonic Dipolar Anti-Bonding Mode in Silver Nanoring Structures. *Nanotechnology* **2009**, *20*, 465203.
50. Zener, C. Non-Adiabatic Crossing of Energy Levels. *Proc. R. Soc. London, Ser. A* **1932**, *137*, 696–702.
51. Hao, F.; Larsson, E. M.; Ali, T. A.; Sutherland, D. S.; Nordlander, P. Shedding Light on Dark Plasmons in Gold Nanorings. *Chem. Phys. Lett.* **2008**, *458*, 262–266.